Electrochimica Acta 64 (2012) 130–139

Contents lists available at SciVerse ScienceDirect

Electrochimica Acta

journal homepage: www.elsevier.com/locate/electacta

Physical interpretation of cyclic voltammetry for measuring electric double layer capacitances

Hainan Wang, Laurent Pilon*

University of California, Los Angeles, Henry Samueli School of Engineering and Applied Science, Mechanical and Aerospace Engineering Department, 420 Westwood Plaza, Los Angeles, CA 90095, USA

ARTICLE INFO

Article history:
Received 29 October 2011
Received in revised form
28 December 2011
Accepted 29 December 2011
Available online 8 January 2012

Keywords:
Cyclic voltammetry
Electric double layer
Electrochemical capacitor
Electric double layer capacitor
Modified Poisson–Nernst–Planck model
Dimensional analysis

ABSTRACT

This paper aims to develop a model for simulating the electric double layer dynamics in CV measurements while simultaneously accounting for transport phenomena in both the electrode and the electrolyte. It also aims (i) to identify the dimensionless parameters that govern the CV measurements, (ii) to provide a physical interpretation of the shape of CV curves, and (iii) to investigate the effect of the electrode electrical conductivity on the predicted double layer capacitance. The transient double layer dynamics was simulated using the modified Poisson–Nernst–Planck (MPNP) model with a Stern layer and accounting for the presence of the electrode. A dimensional analysis was performed and four dimensionless numbers governing the CV measurements were identified. This study established that the hump in CV curves for electrodes with large radius of curvature was due to the saturation of ion concentration near the electrode surface before reaching the maximum potential. It also demonstrates that CV curves became symmetric for large ion diffusion coefficient due to rapid ion transport. This study confirmed that the EDL capacitance retrieved from CV measurements is constant for low scan rates and corresponds to the capacitance under equilibrium conditions. Larger ion diffusion coefficient and electrode electrical conductivity led to larger EDL capacitance at large scan rates corresponding to better charging performance.

1. Introduction

Cyclic voltammetry (CV) is a powerful tool in the field of electrochemistry [1,2]. It has been used extensively to characterize the performance of various electrical energy storage devices such as electrochemical capacitors (also known as supercapacitors) [3–5], batteries [6,7], and fuel cells [8,9]. In these applications, the charged electrodes are typically immersed in the electrolyte solution. Electric double layers form at the electrode/electrolyte interfaces which are accessible to ions present in the electrolyte. Fig. 1 shows a schematic of the electric double layer structure forming near the surface of an anode. Solvated cations of diameter a migrate and adsorb to the electrode surface due to electrostatic forces [1,10–12]. The Stern layer is defined as the compact layer of immobile ions strongly adsorbed to the electrode surface [1,10–12]. Note that there are no free charges within the Stern layer [1,10,11]. Beyond the Stern layer is the so-called diffuse layer where ions are mobile under the coupled influence of electrostatic forces and diffusion [1,10–12]. Fig. 1b shows the electric circuit representation of an electric double layer capacitance including the electrode resistance, the Stern layer and diffuse layer capacitances in series [1,3,10,12].

CV measurements consist of imposing an electric potential at the electrodes which varies periodically and linearly with time [1,2]. The resulting electric current is recorded. The total charge accumulated at the electrode surface can be found by integrating the electric current with respect to time [3,13–16]. Then, the capacitance can be estimated as the total charge divided by the "potential window" [3,14–17]. Capacitance is typically measured at different scan rates to characterize the performance of energy storage devices such as electric double layer capacitors (EDLCs) [3–5,13–17]. The capacitance measured at low scan rates is maximum and close to the capacitance under equilibrium conditions.

Moreover, the shape of CV curves has been used extensively to deduce the electrochemical processes involved in the charging and discharging of EDLCs [18–22]. For example, the current initially increases when charging EDLCs from zero potential. Then, it decreases upon further increase in the electric potential. Thus, a "hump" is typically observed in the CV curves. Different interpretations have been proposed in the literature to explain this observation. For example, Pell et al. [23] investigated the effect of the electrolyte concentration on the charging/discharging of EDLCs. The electrode was carbon foil formed using carbon powders while the electrolyte was tetraethylammonium tetrafluoroborate

* Corresponding author. Tel.: +1 310 206 5598; fax: +1 310 206 2302.
E-mail address: pilon@seas.ucla.edu (L. Pilon).

0013-4686/$ – see front matter © 2012 Elsevier Ltd. All rights reserved.
doi:10.1016/j.electacta.2011.12.118

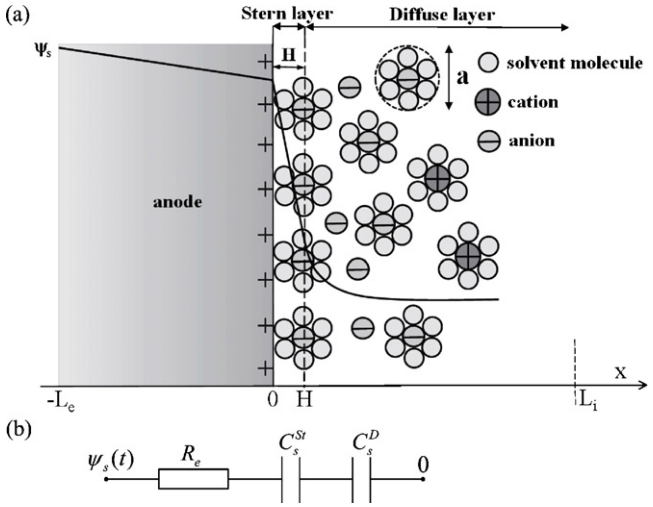

Fig. 1. Schematic of (a) the electric double layer structure showing the arrangement of solvated anions and cations near an anode/electrolyte interface and the simulated computational domain consisting of a Stern layer and the diffuse layer and (b) the electrode resistance along with the Stern and diffuse layer capacitances in series [10,1,3].

(TEATFB) in propylene carbonate with concentration ranging from 0.08 to 1 mol/L. The authors observed a hump in CV curves at low electrolyte concentration of 0.08 mol/L which was absent at larger ones. Consequently, the authors attributed its reason to the "*electrolyte starvation*" due to limited amount of ions at low concentrations. The same interpretation was suggested for EDLCs with both aqueous (H_2SO_4) and organic ($TEABF_4$) electrolytes with 1 mol/L concentration [24]. Moreover, the hump was also attributed to redox reactions at the electrode surface [4,25–34] as well as the "*difference of diffusion capability between solvated anions and cations in the electrolyte*" [32]. Recently, Mysyk et al. [35,36] experimentally investigated this effect for EDLCs with electrodes made of pitch-derived and viscose-based carbons in both aqueous and organic electrolytes. The authors systematically measured the CV curves for these carbon electrodes featuring different specific surface area and pore size. They observed the hump for carbon electrodes with small pore size in electrolytes with large ion size. Thus, they speculated that the "*available active surface becomes fully saturated with ions*" before reaching the maximum potential. Then, the current began to decrease even as the potential further increased. However, there is still no clear and definitive explanations to this observed phenomenon. In addition, to the best of our knowledge, no studies have attempted to elucidate this question using physics-based numerical simulations.

This paper aims to develop a model for simulating electric double layer capacitors by accounting for transport phenomena in both the electrode and the electrolyte under large potential and with concentrated electrolyte solutions. It also aims to provide physical interpretations of CV measurements used to determine electric double layer capacitance.

2. Background

2.1. Cyclic voltammetry

In CV measurements, the electrode surface potential is imposed to vary periodically and linearly with time as,

$$\psi_s(t) = \begin{cases} \psi_{min} + vt & \text{for } 2(n-1)t_0 \le t < (2n-1)t_0 \quad \text{(a)} \\ \psi_{max} - v[t-(2n-1)t_0] & \text{for } (2n-1)t_0 \le t < 2nt_0 \quad \text{(b)} \end{cases} \tag{1}$$

where v is the scan rate in V/s, $n(=1, 2, 3, \ldots)$ is the cycle number, and $t_0 = (\psi_{max} - \psi_{min})/v$ is half the cycle period. It represents the time for the surface potential to vary from its minimum (ψ_{min}) to its maximum (ψ_{max}) values or versa vice. Here, $\Delta\psi = \psi_{max} - \psi_{min}$ is referred to as the "potential window". The charge per unit surface area (or surface charge density) q_s accumulated at the electrode surface during one cycle can be found by integrating the current density j_s (in A/m^2) at the electrode surface with respect to time as [3,13–17,23],

$$q_s = \frac{1}{2}\int_{2(n-1)t_0}^{2nt_0} j_s dt = \frac{1}{2}\oint \frac{j_s}{v} d\psi \tag{2}$$

Then, the capacitance per unit surface area (or specific capacitance) can be estimated from CV measurements as [3,14–17],

$$C_s = \frac{q_s}{\psi_{max} - \psi_{min}} \tag{3}$$

2.2. Numerical simulations of cyclic voltammetry

Numerous studies have simulated CV measurements of electric double layers. These simulations were based on either equivalent RC circuit models [13,37–39] or the classical Poisson–Nernst–Planck (PNP) model [2,40–42]. However, these models suffer from severe limitations. First, the classical RC circuit models inherently neglects ion diffusion and non-uniform ion concentration in the electrolyte [43–46]. These models may not be valid for EDLCs under large electric potential and electrolyte concentration [43–47]. Second, the PNP model neglects the finite size of ions and treated as point-charges [45,46,48,49]. This assumption breaks down when either the electrolyte concentration c_∞ or the electric potential is large [46,48,49]. Therefore, the PNP model is invalid for practical EDLCs with typical electrolyte concentration larger than 1 mol/L and electric potential larger than 1 V. Moreover, the effects of electrodes were typically neglected in simulating CV measurements using the PNP model [2,40–42]. However, studies have demonstrated that the electrode electrical conductivity significantly affected the charging performance of EDLCs [50–54].

Efforts have been made in recent literature to account for the effect of finite ion size in modeling ion transport in concentrated electrolyte solutions under large electric potential [45,48,49]. For example, Kilic et al. [48] derived a modified PNP (MPNP) model valid for binary and symmetric electrolytes under large electrolyte concentration and electric potential. The authors added an excess term in the expression of the electrochemical potential to account for the finite ion size [45,48,49]. However, to the best of our knowledge, no studies have simulated CV measurements for electric double layers under large electrolyte concentrations and electric potential other than by using RC circuit models [2,13,37–41]. Given the limitations of the latter, it is important to develop a model that can simulate CV measurements under practical conditions and account for the presence of the electrode in simulating the charging/discharging of EDLCs. This model will be useful to identify the important parameters affecting the performance of EDLCs and to elucidate the electrochemical processes involved.

This paper aims to develop a model for simulating the electric double layer dynamics in CV measurements while simultaneously accounting for transport phenomena in both the electrode and the electrolyte. It also aims (i) to identify the dimensionless parameters that govern the CV measurements, (ii) to provide a physical interpretation of the shape of CV curves, and (iii) to investigate the effect of the electrode electrical conductivity on the predicted double layer capacitance. The dynamics of the electric double layer forming near a planar electrode in aqueous electrolyte solutions during CV measurements was simulated as a function of scan rate. A modified PNP model with a Stern layer [45,46,48,49] was used while simultaneously accounting for the electrode. The results were

compared with analytical expressions for the capacitances under equilibrium conditions.

3. Analysis

3.1. Schematics and assumptions

Fig. 1 shows the schematic of the computational domain used to simulate a planar electrode of thickness L_e immersed in an electrolyte solution. The region of electrolyte solution consists of two layers corresponding to (1) a Stern layer of thickness H near the electrode surface and (2) a diffuse layer beyond. A time-dependent electric potential $\psi_s(t)$ was prescribed at the electrode surface ($x=-L_e$) and was zero far away from the electrode surface ($x=L_i$). The electrode thickness L_e and the length of the electrolyte domain $L_i$were specified to be $L_e=0$ or 100 nm and $L_i=80$ nm, respectively. Here, the length L_i corresponded to half of the distance between the anode and the cathode. Both the electric potential and the electrolyte concentration remained unchanged at the middle plane ($x=L_i$) when L_i was much larger than the double layer thickness [43,55–57]. Thus, it sufficed to simulate only half of the domain by imposing zero electric potential and bulk electrolyte concentration c_∞ at $x=L_i$. In addition, the electric double layer thickness decreases with increasing electrolyte concentration [1,10–12,48,49]. Increasing the value of L_i by a factor of two was found to have no effect (i) on the predicted specific capacitance under equilibrium conditions and (ii) on the capacitance C_s and j_s versus ψ_s curves retrieved from CV simulations at low scan rates defined by Eqs. (3) and (12), respectively. However, the values of C_s predicted at large scan rates were found to decrease with increasing L_i. In addition, the j_s versus ψ_s curves predicted at large scan rates became more asymmetric as L_i increased as discussed in Section 4.4. These can be attributed to the fact that the charge storage took longer as it could not follow the fast variation in the electric potential under large scan rates when the electrolyte domain length L_i increased [43,46,55].

To make the problem mathematically tractable, the following assumptions were made: (1) anions and cations had the same effective diameter and diffusion coefficient which were assumed to be constant and independent of electrolyte concentration [48,49,58], (2) the electrolyte dielectric permittivity was constant and equals to that of water, (3) isothermal conditions prevailed throughout the electrode and electrolyte, (4) advection of the electrolyte was assumed to be negligible, (5) the ions could only accumulate at the electrode surface and could not diffuse into the electrode, i.e., there was no ion insertion, and (6) the specific ion adsorption due to non-electrostatic forces were assumed to be negligible.

3.2. Dimensional analysis and formulation

The local electric potential $\psi(x,t)$ in the electrode was governed by the Poisson equation [59–65]. In the absence of the electric current caused by redox reactions [assumption (5)], it is expressed as [61–65],

$$\frac{\partial}{\partial x}\left(\sigma_e\frac{\partial\psi}{\partial x}\right)=0 \quad \text{for} \quad -L_e\le x<0 \tag{4}$$

where σ_e is the electrical conductivity of the electrode material expressed in S/m. Moreover, the local electric potential $\psi(x,t)$ and ion concentrations $c_i(x,t)$ at time t and location x in the electrolyte solution were computed by solving the MPNP model with a Stern layer for large electrolyte concentration [45,46,48,49]. For binary and symmetric electrolytes, the valency is such that $z_1=-z_2=z$ and the bulk ion concentration is given by $c_{1\infty}=c_{2\infty}=c_\infty$. Then, assuming identical diffusion coefficient $D_1=D_2=D$, the MPNP model with Stern layer can be written as [45,46,48,49],

$$\frac{\partial}{\partial x}\left(\epsilon_0\epsilon_r\frac{\partial\psi}{\partial x}\right)=\begin{cases}0 & \text{for} \quad 0\le x<H \quad \text{(a)}\\ eN_Az(c_1-c_2) & \text{for} \quad x\ge H \quad \text{(b)}\end{cases}$$

$$\frac{\partial c_i}{\partial t}=\frac{\partial}{\partial x}\left(D\frac{\partial c_i}{\partial x}+\frac{z_iD}{R_uT}Fc_i\frac{\partial\psi}{\partial x}+\frac{\nu Dc_i}{2c_\infty-\nu(c_1+c_2)}\frac{\partial(c_1+c_2)}{\partial x}\right) \quad \textit{for} \quad x\ge H \quad \text{(c)} \tag{5}$$

where $c_i(x,t)$ is the local molar concentration of ion species "i" ($i=1$, 2) while ϵ_0 and ϵ_r are the free space permittivity ($\epsilon_0=8.854\times10^{-12}$ F/m) and the relative permittivity of the electrolyte solution, respectively. The absolute temperature is denoted by T, e is the elementary charge ($e=1.602\times10^{-19}$ C), N_A is the Avogadro's number ($N_A=6.022\times10^{23}$ mol^{-1}) while F and R_u are the Faraday constant ($F=eN_A$ sA/mol) and the universal gas constant ($R_u=8.314$ JK^{-1}mol^{-1}), respectively. The packing parameter is defined as $\nu=2a^3N_Ac_\infty$ where a is the effective ion diameter. It represents the ratio of the total bulk ion concentration to the maximum ion concentration $c_m=1/N_Aa^3$ assuming a simple cubic packing [45,49,66]. Therefore, ν should not be larger than unity for the model to be physically acceptable [45,49,66]. Eqs. (5b) and (5c) reduce to the classical Poisson–Nernst–Planck model when $\nu=0$ [45,48,49]. Note that in Refs. [45,48,49], the Stern layer was accounted for via a boundary condition relating the potential drop across the Stern layer and the potential gradient at the Stern/diffuse layer interface. Here, the electric potential in the Stern layer was solved explicitly. In fact, these two approaches are equivalent for planar electrodes [45,46,48,67].

Moreover, the surface electric potential $\psi_s(t)$ expressed by Eq. (1) was imposed, i.e.,

$$\psi=\psi_s(t), \quad \text{at} \quad x=-L_e \tag{6a}$$

The electric potential and current density were continuous across the electrode/electrolyte interface located at $x=0$ nm so that [68],

$$\psi|_{x=0^-}=\psi|_{x=0^+} \quad \text{and} \quad -\sigma_e\frac{\partial\psi}{\partial x}\Big|_{x=0^-}=-\epsilon_0\epsilon_r\frac{\partial^2\psi}{\partial x\partial t}\Big|_{x=0^+} \tag{6b}$$

Similarly, the electric potential and displacement were continuous across the Stern/diffuse layer interface located at $x=H$ [10,69,46],

$$\psi\Big|_{x=H^-}=\psi\Big|_{x=H^+} \quad \text{and} \quad \epsilon_0\epsilon_r\frac{\partial\psi}{\partial x}\Big|_{x=H^-}=\epsilon_0\epsilon_r\frac{\partial\psi}{\partial x}\Big|_{x=H^+}, \tag{6c}$$

In addition, the mass flux vanishes for both ion species at the electrode surface since there is no ion insertion [assumption (5)] planar electrodes [45,46,48,49],

$$D\frac{\partial c_i}{\partial x}+\frac{z_iD}{R_uT}Fc_i\frac{\partial\psi}{\partial x}+\frac{\nu Dc_i}{2c_\infty-\nu(c_1+c_2)}\frac{\partial(c_1+c_2)}{\partial x}=0, \quad \text{at} \quad x=H \tag{6d}$$

Far away from the electrode surface, the electric potential and ion concentration are such that,

$$\psi(x=L_i,t)=0 \quad \text{and} \quad c_i(x=L_i,t)=c_\infty, \tag{6e}$$

Finally, the initial conditions are given by,

$$\psi(x,t=0)=0 \quad \text{and} \quad c_i(x,t=0)=c_\infty, \quad \textit{for} \quad 0\le x\le L_i \tag{6f}$$

Note that, when $L_e=0$ nm, Eqs. (4)–(6) correspond to simulations without accounting for the presence of the electrode.

The following scaling parameters were introduced to make the formulation dimensionless,

$$\psi^*=\frac{\psi}{\psi_{max}-\psi_{min}}, \quad x^*=\frac{x}{L_i}, \quad t^*=\frac{tD}{L_i^2}, \quad c_i^*=\frac{c_i}{c_\infty}, \quad j_s^*=\frac{j_s}{2zeN_ADc_\infty/L_i} \tag{7}$$

Then, the governing Eqs. (4)–(6) were transformed into dimensionless form as,

$$\frac{\partial^2\psi^*}{\partial x^{*2}} = 0 \quad \text{for} \quad -L_e/L_i \le x^* < 0 \qquad \text{(a)}$$

$$\frac{R_uT/zF}{\psi_{max}-\psi_{min}}\left(\frac{\lambda_D}{L_i}\right)^2\frac{\partial^2\psi^*}{\partial x^{*2}} = \begin{cases} 0 & \text{for} \quad 0 \le x^* < H/L_i \quad \text{(b)} \\ \frac{1}{2}(c_1^*-c_2^*) & \text{for} \quad x^* \ge H/L_i \quad \text{(c)} \end{cases} \tag{8}$$

$$\frac{\partial c_i^*}{\partial t^*} = \frac{\partial}{\partial x^*}\left(\frac{\partial c_i^*}{\partial x^*} + \frac{R_uT/zF}{\psi_{max}-\psi_{min}}\mathrm{sgn}(z_i)c_i\frac{\partial\psi^*}{\partial x^*} + \frac{\nu c_i^*}{2-\nu(c_1^*+c_2^*)}\frac{\partial(c_1^*+c_2^*)}{\partial x^*}\right)$$

$$\text{for} \quad x^* \ge H/L_i \qquad \text{(d)}$$

The associated dimensionless boundary and initial conditions [Eqs. (6)] became,

$$\psi^*(t^*) = \Pi_3 t^*, \quad \text{at} \quad x^* = -L_e/L_i \tag{9a}$$

$$\psi^*\big|_{x^*=0^-} = \psi^*\big|_{x^*=0^+} \quad \text{and} \quad \frac{\sigma_e(\psi_{max}-\psi_{min})/L_e}{2zeN_ADc_\infty/L_i}\frac{L_e}{L_i}\frac{\partial\psi^*}{\partial x^*}\Big|_{x^*=0^-} = \frac{\psi_{max}-\psi_{min}}{R_uT/zF}\left(\frac{\lambda_D}{L_i}\right)^2\frac{\partial^2\psi^*}{\partial x^*\partial t^*}\Big|_{x^*=0^+} \tag{9b}$$

$$\psi^*\big|_{x^*=(H/L_i)^-} = \psi^*\big|_{x^*=(H/L_i)^+} \quad \text{and} \quad \frac{\partial\psi^*}{\partial x^*}\Big|_{x^*=(H/L_i)^-} = \frac{\partial\psi^*}{\partial x^*}\Big|_{x^*=(H/L_i)^+}, \tag{9c}$$

$$\frac{\partial c_i^*}{\partial x^*} + \frac{R_uT/zF}{\psi_{max}-\psi_{min}}\mathrm{sgn}(z_i)c_i\frac{\partial\psi^*}{\partial x^*} + \frac{\nu c_i^*}{2-\nu(c_1^*+c_2^*)}\frac{\partial(c_1^*+c_2^*)}{\partial x^*}, \quad \text{at} \quad x^* = H/L_i \tag{9d}$$

$$\psi^*(x^*=1,t^*)=0 \quad \text{and} \quad c_i^*(x^*=1,t^*)=1, \tag{9e}$$

$$\psi^*(x^*,t^*=0)=0 \quad \text{and} \quad c_i^*(x^*,t^*=0)=1, \quad \text{for} \quad 0 \le x^* \le 1 \tag{9f}$$

Here, four key dimensionless numbers were identified in Eqs. (8) and (9) as

$$\Pi_1 = \frac{R_uT/zF}{\psi_{max}-\psi_{min}}, \quad \Pi_2 = \frac{\lambda_D}{L_i}, \quad \Pi_3 = \frac{\nu L_i^2/D}{\psi_{max}-\psi_{min}}, \quad \text{and}$$

$$\Pi_4 = \frac{\sigma_e(\psi_{max}-\psi_{min})/L_e}{2zeN_ADc_\infty/L_i} \tag{10}$$

where Π_1 represents the ratio of thermal potential (R_uT/zF) and the potential window in CV measurements. The dimensionless number $\Pi_2 = \lambda_D/L_i$ is the ratio of Debye length and the thickness of electrolyte layer while Π_3 is the dimensionless scan rate. Here, the Debye length for symmetric electrolytes is defined as $\lambda_D = (\epsilon_0\epsilon_r R_uT/2e^2z^2N_A^2c_\infty)^{1/2}$ [1,10–12]. The dimensionless number Π_4 represents the ratio of the characteristic current densities in the electrode and in the electrolyte.

Note that the thermal voltage R_uT/F can also be used as a characteristic potential in the electric double layers. This has been done frequently to scale the electric potential in the electrolyte [43–45,48,49,57,66]. However, R_uT/F is not a characteristic potential in the electrodes since the governing equation for the electric potential [Eq. (4)] is independent of temperature. By contrast, the potential window ($\psi_{max}-\psi_{min}$) is a realistic and important parameter in the CV measurements and thus was used as the characteristic potential in the present study. It is interesting to note that when R_uT/F is used to scale the electric potential, the associated set of dimensionless numbers, denoted by Π_1' to Π_4', is a combination of Π_1 to Π_4 given by Eq. (10), namely, $\Pi_1' = 1/\Pi_1$, $\Pi_2' = \Pi_2$, $\Pi_3' = \Pi_3/\Pi_1$, and $\Pi_4' = \Pi_1\Pi_4$. Thus, both approaches are consistent with one another and lead to the same dimensionless numbers.

3.3. Constitutive relations

In order to solve Eqs. (8) and (9), the electrode conductivity σ_e and electrolyte properties ϵ_r, z, c_∞, a and D along with the temperature T and the surface potential $\psi_s(t)$ are needed. The electrical conductivity of activated carbons is on the order of 10^{-6} to 10^2 S/m [50,53]. Here, the electrode electrical conductivity was taken as $\sigma_e = 10$ or 0.01 S/m. The present study focuses on aqueous electrolyte solution at room temperature so that $T = 298$ K with $\epsilon_r = 78.5$ [70]. The effective ion diameter and diffusion coefficient were taken as $a = 0.66$ nm [58] and $D = 2\times10^{-9}$ m^2/s [70], respectively, while the valency was $z = 1$. These values correspond to solvated ions such as K^+ and Cl^- in aqueous solutions [58,70]. The electrolyte concentration was chosen as $c_\infty = 1.0$ mol/L corresponding to typical values in actual EDLCs. In addition, the Stern layer thickness H was approximated as the radius of solvated ions, i.e., $H = a/2 = 0.33$ nm [1,11,12]. Moreover, in the surface electric potential $\psi_s(t)$ [Eq. (1)], ψ_{max} was varied from 0.3 to 0.5 V while $\psi_{min} = 0.0$ V. The case of $\psi_{max} = 0.5$ V corresponds to a typical potential difference of 1.0 V between the anode and the cathode typical of aqueous EDLCs.

Finally, a parametric study was carried out for scan rate ν ranging from 10^2 to 10^9 V/s to explore the limiting behaviors of electric double layers. These scan rates were several orders of magnitude larger than those encountered in CV measurements of actual EDLCs with mesoporous electrodes which typically range from 0.001 to 200 V/s [5,18–22]. The difference was due to (i) the small electrode thickness L_e and the small electrical resistance of planar electrodes compared with that of mesoporous electrodes and (ii) the small electrolyte thickness L_i and thus the small ionic resistance [Eq. (14)] compared with that in actual EDLCs. A parametric study was also carried out for other values of diffusion coefficient, namely, $D = 2\times10^{-10}$ to 2×10^{-7} m^2/s.

3.4. Method of solution and data processing

The models were solved using the commercial finite element solver COMSOL 4.1. The capacitance under equilibrium conditions and the capacitance retrieved from CV simulations were computed as follows.

3.4.1. Capacitance under equilibrium conditions

The capacitance under equilibrium conditions corresponds to the time-independent surface potential, i.e., $\psi_s(t) = \psi_{max}$. Then, the Stern and diffuse layer specific capacitances C_s^{St} and C_s^D are defined by dividing the surface charge density [11,60] $q_s(x) = \epsilon_0\epsilon_r E(x)$ by their respective potential difference [1,67,69]. Here, $E(x) = |-d\psi/dx|$ is the norm of the local electric field. The capacitances C_s^{St} and C_s^D of planar electrodes assuming constant electrolyte properties and accounting for the finite ion size are given by [1,49,66,67,69],

$$C_s^{St} = \frac{\epsilon_0\epsilon_r}{H} \tag{11a}$$

$$C_s^D = \frac{2zeN_Ac_\infty\lambda_D}{\psi_D}\sqrt{\frac{2}{\nu}\log\left[1+2\nu\sinh^2\left(\frac{ze\psi_D}{2k_BT}\right)\right]} \tag{11b}$$

where $\psi_D = \psi(H)$ is the electric potential computed at the Stern layer/diffuse layer interface $x = H$. Here, it was obtained by solving the steady-state equilibrium modified Poisson–Boltzmann (MPB) model at surface potential ψ_{dc} and electrolyte concentration c_∞ [48,49,66,67]. Then, the total specific capacitance C_s under equilibrium conditions was calculated using the series formula as [1,67,69],

$$\frac{1}{C_s} = \frac{1}{C_s^{St}} + \frac{1}{C_s^D} \tag{12}$$

Numerical convergence study was performed as discussed in Refs. [46,67]. The maximum mesh size was specified to be 0.01 nm at the electrode surface and 1 nm in the rest of the domain.

3.4.2. Simulating CV measurements

CV measurements were simulated by numerically imposing the periodic surface electric potential given by Eq. (1). The dimensionless governing Eqs. (8) were solved along with the boundary and

initial conditions given by Eqs. (9). The corresponding transient surface current density was estimated as [57,59,60,71–76],

$$j_s^*(t^*) = \Pi_4 \frac{L_e}{L_i} \frac{\partial \psi^*}{\partial x^*}\Big|_{x^*=0^-} = \Pi_1 \left(\frac{\lambda_D}{L_i}\right)^2 \frac{\partial^2 \psi^*}{\partial x^* \partial t^*}\Big|_{x^*=0^+} \quad (13)$$

Simulations of CV measurements were run for at least 5 periods (i.e., $t \geq 10t_0$) to ensure the current density had reached its stationary and periodic states. Then, the surface charge density $q_s(t)$ was estimated by Eq. (2) and the specific capacitance C_s was computed using Eq. (3). The numerical convergence criterion was defined such that the maximum relative difference in the retrieved value of C_s was less than 1% when (1) reducing the mesh size by a factor five, (2) dividing the time step by five, and (3) running the CV simulations for 5 more periods. The time step was imposed to be $\Delta t \approx t_0/1000 = (\psi_{max} - \psi_{min})/1000\nu$. Note that this time step decreased with increasing scan rate ν and was several orders of magnitude smaller than the characteristic time for diffusion L_i^2/D. In addition, further reduction in the time step below the Debye relaxation time λ_D^2/D was also found to have no effect on the predicted values of j_s and C_s. The mesh size was the smallest at the electrode surface due to large potential gradient and then gradually increased. The maximum mesh size was specified to be 0.001 nm at the electrode surface and 1 nm in the rest of the domain. The total number of finite elements was less than 400 for all cases simulated in the present study.

3.4.3. Validation

The numerical tool was validated based on three equilibrium and transient cases reported in the literature. First, the equilibrium electric potential profile in the diffuse layer predicted by solving the MPB model was validated against the exact solution for planar electrodes [10,11,69] with $\epsilon_r = 78.5$, $c_\infty = 0.01$ and 0.001 mol/L, $\nu = 0$, and $\psi_D = 0.1$ V. Second, the computed specific capacitances for the Stern and diffuse layers obtained from the MPB model were validated against Eqs. (11a) and (11b) for (i) $\psi_s = 0.1$ V, $c_\infty = 0.01$ mol/L, and $a = 0.66$ nm as well as (ii) $\psi_s = 0.5$ V, $c_\infty = 1$ mol/L, and $a = 0.66$ nm. Third, the transient ion concentration and electric potential profiles predicted by solving the PNP and MPNP models with constant surface potential were compared with the numerical solutions for planar electrodes reported in Ref. [48]. Comparison was made against the reported values of $c_i(x, t)$ and $\psi(x, t)$ for a wide range of packing parameter ν and dimensionless potential ($zF\psi_D/R_uT$) [48]. Good agreement was obtained between our results and reported values for all cases considered.

4. Results and discussion

4.1. Dimensional analysis

Fig. 2(a) shows the predicted current density j_s versus surface potential ψ_s ($j_s - \psi_s$ curves) obtained from CV simulations for three cases featuring different values of T, L_i, a, c_∞, D, ν, and ψ_{max} as summarized in Table 1. However, the dimensionless numbers for all cases were identical, namely, $\Pi_1 = 19.47$, $\Pi_2 = 0.0038$, $\Pi_3 = 64$, and $\Pi_4 \to \infty$. Results were obtained by numerically solving the MPNP model with a Stern layer [Eqs. (8) and (9)] without electrode, i.e., $L_e = 0$ nm. Fig. 2(a) shows that the predicted $j_s - \psi_s$ curves

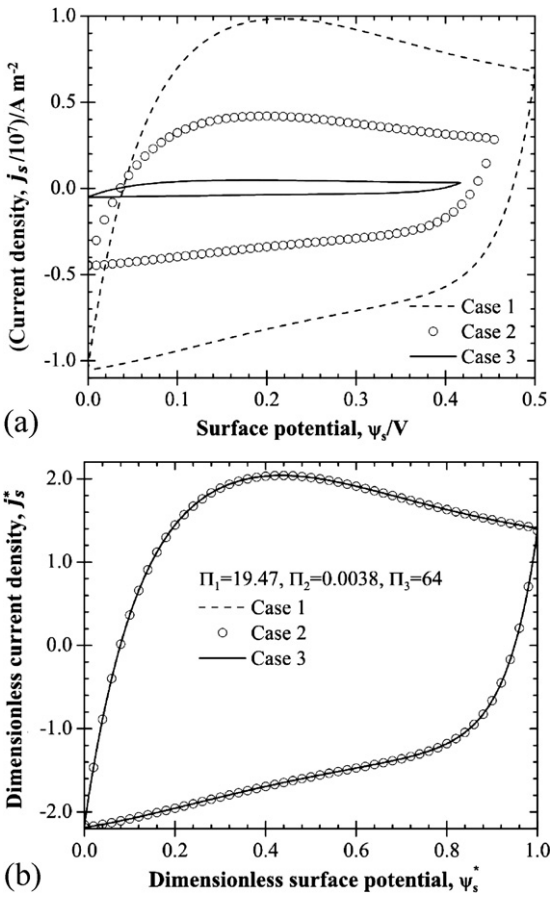

Fig. 2. Predicted (a) j_s versus ψ_s curves and (b) j_s^* versus ψ_s^* curves from CV simulations for three cases with parameters given in Table 1. Results were obtained by numerically solving the MPNP model with a Stern layer [Eqs. (8) and (9)] without accounting for the electrode ($L_e = 0$ nm) with $\Pi_1 = 19.47$, $\Pi_2 = \lambda_D/L_i = 0.0038$, $\Pi_3 = 64$, and $\Pi_4 \to \infty$.

were significantly different for these three cases. However, Fig. 2(b) demonstrates that the dimensionless $j_s^* - \psi_s^*$ curves overlapped after using the scaling parameters defined by Eq. (7). Overall, these results demonstrate that (i) the scaling parameters defined by Eq. (7) and the dimensional analysis for CV simulations were valid and (ii) the double layer charging dynamics near planar electrodes in CV measurements was governed by four dimensionless numbers, i.e., Π_1, Π_2, Π_3, and Π_4 given by Eq. (10).

4.2. Effect of scan rate

Fig. 3(a) and (b) shows the numerically predicted $j_s^* - \psi_s^*$ curves from CV simulations for dimensionless scan rate Π_3 ranging from 0.64 to 64,000. The results were obtained by solving the MPNP model with a Stern layer [Eqs. (8) and (9)] without the electrode ($L_e = 0$ nm). The dimensionless numbers Π_1, Π_2 and Π_4 were identical to those used to produce Fig. 2(b). Fig. 3(a) and (b) demonstrates that the magnitude of the current density j_s^* increased significantly with increasing dimensionless scan rate Π_3. This can

Table 1
Parameters in simulations without accounting for the electrode ($L_e = 0$ nm or $\sigma_e \to \infty$) and such that $\Pi_1 = 19.47$, $\Pi_2 = 0.0038$, $\Pi_3 = 64$, and $\Pi_4 \to \infty$.

	T(K)	L_i(nm)	a(nm)	c_∞(mol/L)	D(m^2/s)	ν(V/s)	ψ_{max} (V)
Case 1	298	80	0.66	1.0	2×10^{-9}	10^7	0.5
Case 2	270.9	88	0.726	0.751	1.25×10^{-9}	4.70×10^6	0.455
Case 3	248.3	96	0.792	0.579	2×10^{-10}	5.79×10^5	0.417

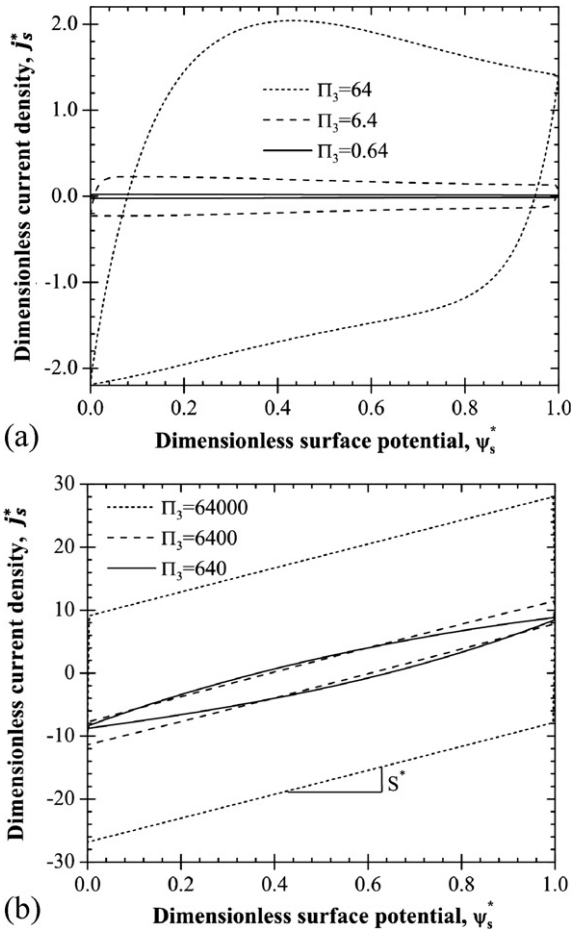

Fig. 3. Predicted j_s^* versus ψ_s^* curves from CV simulations for dimensionless scan rate ranging from (a) $\Pi_3 = 0.64 - 64$ and (b) $\Pi_3 = 640 - 64000$. Results were obtained by numerically solving the MPNP model with a Stern layer [Eqs. (8) and (9)] without accounting for the electrode ($L_e = 0$ nm) with $\Pi_1 = 19.47$, $\Pi_2 = 0.0038$, and $\Pi_4 \to \infty$.

be attributed to the fact that a fast change in the surface potential resulted in a large local electric field and thus a large current density according to Eq. (13). In addition, a "hump" was observed in the $j_s^* - \psi_s^*$ curve for $\Pi_3 = 64$ shown in Fig. 3(a). The hump disappeared when further increasing Π_3 and the $j_s^* - \psi_s^*$ curve became "leaf-like" for $\Pi_3 = 640$ as shown in Fig. 3(b). This is typical of EDLCs at large scan rates corresponding to large resistance to ionic current [4,5,30,34,77]. These trends are similar to those experimentally observed for EDLCs made of porous carbons [4,5,30,34,77]. Moreover, the predicted j_s^* became nearly linearly proportional to the imposed surface potential ψ_s^* for $\Pi_3 > 6400$. In these cases, the electric double layer behaved as a pure resistor [4].

Fig. 4 shows the slope of the $j_s - \psi_s$ curves as a function of dimensionless scan rate Π_3 ranging from 640 to 6.4×10^6. The model and other parameters were identical to those used to produce Fig. 3(b). It is evident that the slope of $j_s - \psi_s$ curves increased with increasing Π_3 and gradually reached a constant plateau for $\Pi_3 \geq 6400$. It is interesting to note that this plateau corresponds to the conductance of an electrolyte solution with ionic conductivity σ_i (in S/m) and thickness L_i given by [72,73,78,79],

$$S = \frac{\sigma_i}{L_i} = \frac{1}{L_i}\frac{F^2}{R_u T}\sum_{i=1}^{2} z_i^2 D_i c_{i\infty} \tag{14}$$

This result confirms that the predicted electrolyte ionic conductivity was indeed equal to the theoretical value when ignoring the electrode contribution to the resistance.

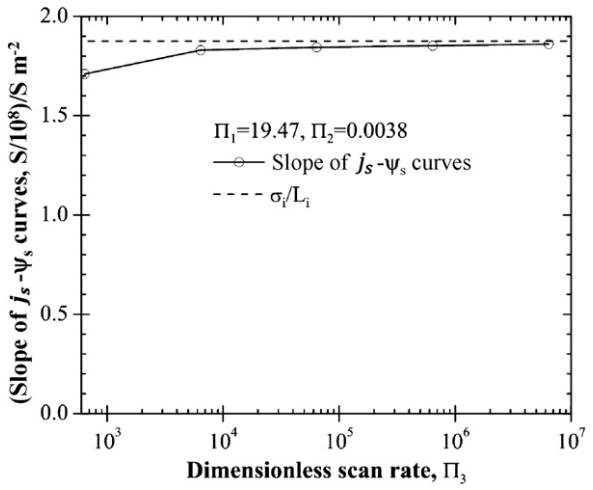

Fig. 4. Slope of the predicted j_s versus ψ_s curves from CV simulations as a function of dimensionless scan rate Π_3. Results were obtained by numerically solving the MPNP model with a Stern layer [Eqs. (8) and (9)] without accounting for the electrode ($L_e = 0$ nm) with $\Pi_1 = 19.47$, $\Pi_2 = 0.0038$, and $\Pi_4 \to \infty$.

4.3. Effect of diffusion coefficient

Fig. 5(a) shows the specific capacitance C_s retrieved from CV simulations using Eq. (3) as a function of scan rate ν ranging from 10^2 to 10^9 V/s. Three values of ion diffusion coefficient were used, i.e., $D = 2 \times 10^{-10}$, 2×10^{-9}, or 2×10^{-8} m^2/s. The model and other parameters were identical to those used in Case 1 and summarized in Table 1. Fig. 5(a) demonstrates that C_s was constant and independent of diffusion coefficient D for scan rate ν smaller than a critical value and decreased rapidly beyond. This critical scan rate increased with increasing ion diffusion coefficient. For scan rates larger than a critical value, ion diffusion becomes a limiting factor in charge storage. Note that the scan rate ν in CV measurements on mesoporous EDLCs typically ranged from 10^{-3} to 200 V/s [5,30,34,77]. The scan rate for planar electrodes considered here was larger due to the small electrical resistance compared with that of mesoporous electrodes.

Fig. 5(b) shows the specific capacitance C_s shown in Fig. 5(a) but plotted as a function of dimensionless scan rate Π_3. It is evident that all the curves now collapsed on a single line for the three different values of diffusion coefficient. Moreover, two regimes can be identified in Fig. 5(b). First, for $\Pi_3 < 1$, ion transport is fast enough to follow the variation in the electric potential $\psi_s(t)$ and the retrieved specific capacitance C_s is independent of scan rate and ion diffusion. In these cases, C_s was equal to $C_s = 87.5$ μF/cm^2. This value was identical to the specific capacitance under equilibrium conditions predicted by Eqs. (11) and (12). Second, for $\Pi_3 > 1$, ion diffusion was the limiting phenomenon for charge storage and C_s decreased with increasing scan rate. Note that similar behavior was also observed in simulating double layer charging dynamics for electrochemical impedance spectroscopy (EIS) in our previous study [46]. However, unlike CV simulations, the capacitance retrieved from EIS predictions did not match the capacitance under equilibrium conditions even at small frequencies [46]. This suggests that CV measurements should be preferred to EIS when measuring the capacitance of EDLCs.

4.4. Interpretation of the hump in CV curves

Fig. 6(a) shows the predicted $j_s^* - \psi_s$ curves from CV simulations for three values of potential window, i.e., $\Delta\psi = 0.3$, 0.4, and 0.5 V. Results were obtained by solving the MPNP model with a Stern layer [Eqs. (8) and (9)] without the electrode ($L_e = 0$ nm). Other

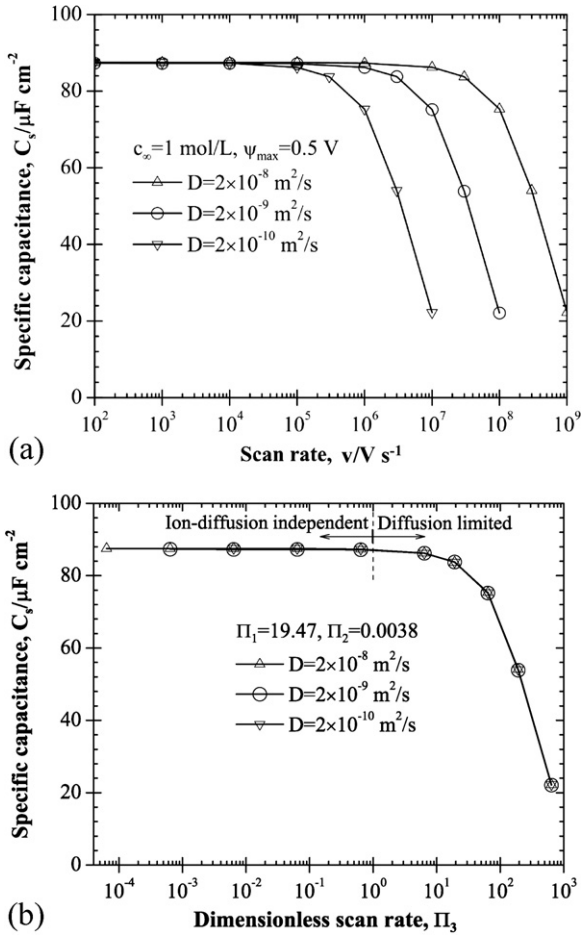

Fig. 5. Predicted specific capacitance C_s from CV simulations as a function of (a) scan rate ν and (b) dimensionless scan rate Π_3. Results were obtained by numerically solving the MPNP model with a Stern layer [Eqs. (8) and (9)] without accounting for the electrode (L_e = 0 nm). The diffusion coefficient D was chosen as $D = 2 \times 10^{-10}$ to 2×10^{-8} m^2/s while Π_1 = 19.47, Π_2 = 0.00380, and $\Pi_4 \to \infty$.

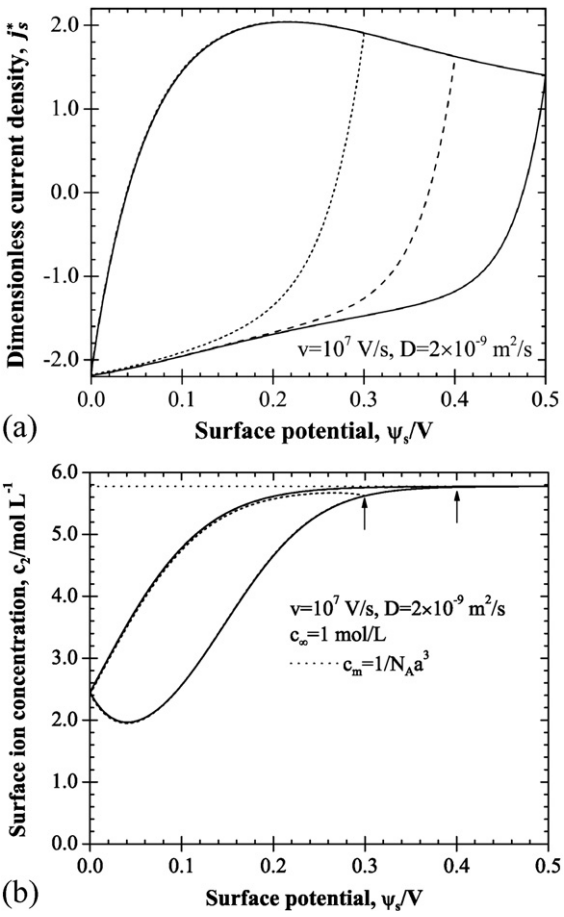

Fig. 6. Predict (a) j_s^* versus ψ_s and (b) $c_2(x = 0) - \psi_s$ curves determined from CV simulations for three values of potential window, i.e., $\psi_{max} - \psi_{min}$ = 0.3, 0.4, and 0.5 V. Results were obtained by numerically solving the MPNP model with a Stern layer [Eqs. (8) and (9)] without accounting for the electrode (L_e = 0 nm) for $\nu = 10^7$ V/s, $D = 2 \times 10^{-9}$ m^2/s, and c_∞ = 1 mol/L.

parameters were identical to those used for Case 1 summarized in Table 1. It is evident that j_s^* reached the maximum value at about ψ_s = 0.2 V for all three curves and then decreased for larger surface potential. Thus, a hump was observed around ψ_s = 0.2 V typical of experimental cyclic voltammetry measurements [4,28–31,35].

Here, the hump was not due to "*electrolyte starvation*" as suggested in Ref. [23] since the electrolyte concentration was large, i.e., c_∞ = 1 mol/L. Moreover, redox reactions were not responsible for the observed hump, as suggested in Refs. [25–34], since only electrostatic phenomenon was accounted for in the present study. Finally, we simulated symmetric electrolytes with identical ion diameter and diffusion coefficient for both cations and anions. Thus, the hump was not due to "*difference of diffusion capability between solvated anions and cations in the electrolyte*" as proposed in Ref. [32].

To physically interpret the observed hump in $j_s - \psi_s$ curves, Fig. 6(b) shows the corresponding anion concentration c_2 at the electrode surface x = 0 nm as a function of surface potential for the same cases considered in Fig. 6(a). The maximum ion concentration $c_m = 1/N_A a^3$ due to finite ion size (Section 3.2) was also plotted in Fig. 6(b). It is evident that the surface anion concentration c_2 increased rapidly with increasing potential up to ψ_s = 0.2 V. This regime corresponded to the increase of current density j_s shown in Fig. 6(a) where it reached a maximum at ψ_s = 0.2 V corresponding to the crest of the hump. For ψ_s > 0.2 V, the anion concentration asymptotically approached its maximum value c_m. Then, the ion accumulation near the electrode surface became slower as the electric potential increased. This, in turn, resulted in the decrease in the current density j_s (Fig. 6(a)). Overall, these results demonstrate that the hump observed experimentally in CV curves for EDLCs can be attributed to the saturation of ion concentration at the electrode surface. This is expected to be valid for relatively large pores or particles so that the effect of electrode curvature is negligible [67,80–83]. In fact, using the equilibrium modified Poisson–Boltzmann model, we have shown that the areal capacitance of spherical particles arranged in SC, FCC, and BCC structures and larger than 100 nm was nearly identical to that of a planar electrode [83,67]. These results and interpretation appear to support those proposed in Refs. [35,36] based on experimental results for large electrolyte concentrations. In addition, a hump was also observed in the predicted $j_s - \psi_s$ curves for small electrolyte concentration c_∞ = 0.05 or 0.1 mol/L (not shown) but at much smaller scan rates than those for larger concentrations. Then, for mesoporous electrodes, the hump observed under small electrolyte concentrations could be also attributed to the saturation of ion concentration in addition to "*electrolyte starvation*". However, the morphology of mesoporous electrodes can significantly affect the charging and discharging of EDLCs [5,18–22]. Therefore, more detailed and systematic simulations accounting for three-dimensional electrode morphology with nanosize pores are essential to further understand the charging performance of mesoporous EDLCs.

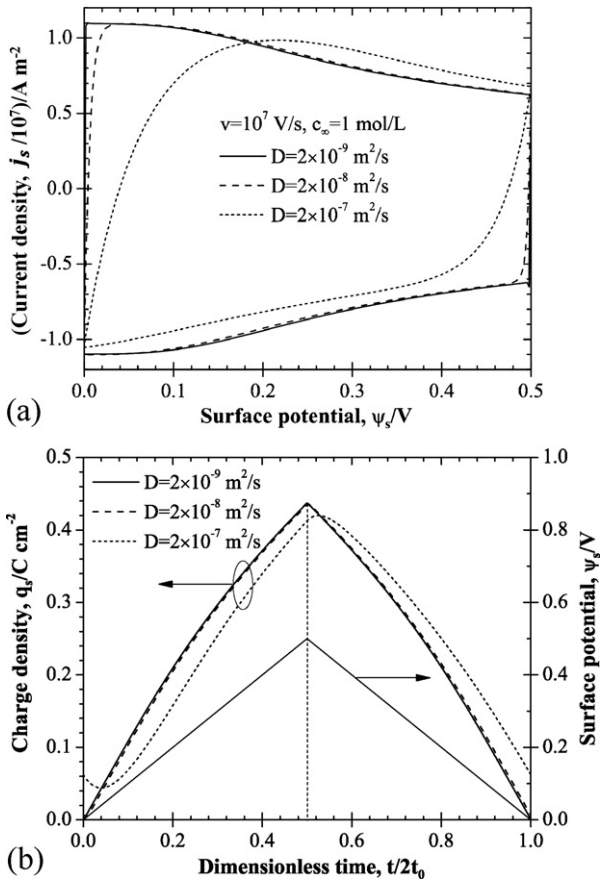

Fig. 7. Plots of (a) j_s versus ψ_s and (b) q_s versus dimensionless time $t/2t_0$ predicted from CV simulations for three values of ion diffusion coefficient, i.e., $D = 2 \times 10^{-9}$, 2×10^{-8}, and 2×10^{-7} m^2/s. Results were obtained by numerically solving the MPNP model with a Stern layer [Eqs. (8) and (9)] without accounting for the electrode ($L_e = 0$ nm) for $v = 10^7$ V/s and $c_\infty = 1$ mol/L.

Finally, Fig. 7(a) shows the $j_s - \psi_s$ curves predicted for three different values of ion diffusion coefficient, i.e., $D = 2 \times 10^{-9}$, 2×10^{-8}, or 2×10^{-7} m^2/s. The potential window was $\Delta\psi = 0.5$ V. The model and other parameters were identical to those used to generate Fig. 6(a) and (b). Fig. 7(a) shows that the hump was observed in the $j_s - \psi_s$ curve for small diffusion coefficient $D = 2 \times 10^{-9}$ m^2/s. However, the hump disappeared when increasing the ion diffusion coefficient to $D = 2 \times 10^{-8}$ and 2×10^{-7} m^2/s. In addition, the $j_s - \psi_s$ curves became nearly symmetric along the line of zero current density $j_s = 0$ A/m^2. It is interesting to note that Lin et al. [21,22] observed a similar trend for EDLCs made of TiC-derived carbons with pore diameter ranging from 0.68 to 1.0 nm in organic electrolytes. The authors attributed the symmetry of CV curves to the reduction in "steric hindering" of ions in large pores, i.e., smaller electrolyte ionic resistance [21,22]. Here, the symmetry in the CV curves can be attributed to the fact that the ion transport can respond nearly instantaneously to the variation in electric potential for large ion diffusion coefficient. This, in turn, leads to smaller ionic resistance according to Eq. (14).

To justify this interpretation, Fig. 7(b) shows the corresponding transient surface charge density $q_s(t) = \epsilon_0 \epsilon_r E_s(t)$ as a function of dimensionless time $t/2t_0$ corresponding to results shown in Fig. 7(a). It also shows the imposed surface potential $\psi_s(t)$. It is evident that the surface charge density $q_s(t)$ responded nearly instantaneously to the surface potential $\psi_s(t)$ for large diffusion coefficient $D = 2 \times 10^{-8}$ and 2×10^{-7} m^2/s. However, there was a lag between $q_s(t)$ and $\psi_s(t)$ for small ion diffusion coefficient $D = 2 \times 10^{-9}$ m^2/s. This confirms that the ion transport was unable to follow the fast variation of surface potential for small diffusion coefficients. In practice, EDLC electrodes are made of mesoporous materials. Then, a large effective ion diffusion coefficient would be beneficial for improving the charging performance and power density of EDLCs. Note that decreasing the electrolyte thickness L_i was found to have the same effect on the predicted $j_s - \psi_s$ curves (Fig. 7(a)) and on q_s versus $t/2t_0$ curves (Fig. 7(b)) as proportionally increasing the ion diffusion coefficient (not shown). Thus, these results justified the choices of the characteristic length L_i and the characteristic time for diffusion L_i^2/D [Eq. (7)] in our dimensional analysis.

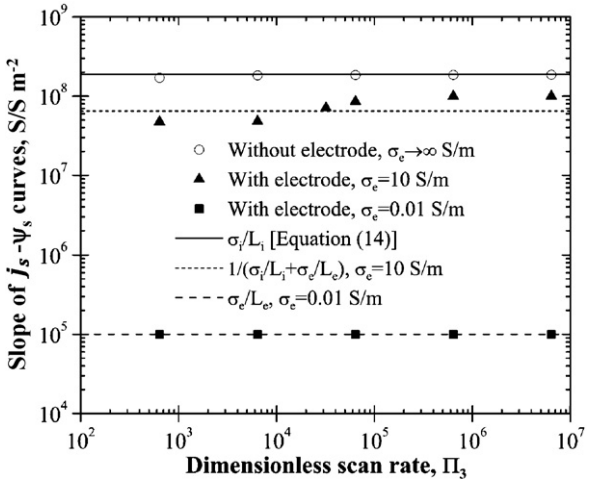

Fig. 8. Slope of the j_s versus ψ_s curves predicted from CV simulations as a function of dimensionless scan rate Π_3 for $\sigma_e \to \infty$, $\sigma_e = 10$, and 0.01 S/m, respectively. Results were obtained by numerically solving the MPNP model with a Stern layer [Eqs. (8) and (9)] accounting for the electrode with $L_i = 80$ nm and $L_e = 100$ nm.

4.5. Effect of the electrode

Previous simulations did not account for the electrode. These simulations corresponded to electrode with zero thickness $L_e = 0$ nm or infinite electrical conductivity $\sigma_e \to \infty$. If taking $\sigma_e = 10$ S/m and $L_e = 100$ nm, the magnitude of the predicted j_s^* was found to decrease by a factor 2 (not shown) compared with results obtained without electrode (Fig. 3(a)). This was due to the increase in the overall electrical resistance of the system.

Fig. 8 shows the slope of the $j_s - \psi_s$ curves from CV simulations as a function of dimensionless scan rate Π_3 for three cases with or without electrode, namely, (i) $\sigma_e \to \infty$ S/m (or $L_e = 0$ nm), (ii) $\sigma_e = 10$ S/m and $L_e = 100$ nm, and (iii) $\sigma_e = 0.01$ S/m and $L_e = 100$ nm. Other parameters were identical to those used to generate Fig. 3(a). Results for the limiting case of $\sigma_e \to \infty$ were taken from Fig. 4. Fig. 8 demonstrates that the slope of $j_s - \psi_s$ curve was dominated by the electrode when its conductivity was small (e.g., $\sigma_e = 0.01$ S/m). For a relatively large electrode conductivity (e.g., $\sigma_e = 10$ S/m), the slope corresponded to the effective conductance of the electrode and electrolyte in series expressed as $(L/\sigma)_{eff} = L_i/\sigma_i + L_e/\sigma_e$.

Finally, Fig. 9 shows the predicted specific capacitance C_s from CV simulations as a function of dimensionless scan rate Π_3 for the three cases considered in Fig. 8. Here again, the value of C_s retrieved from CV curves was constant and equal to $C_s = 87.5$ μF/cm^2 for Π_3 smaller than a critical value which depended on σ_e. Then, it was identical to the specific capacitance under equilibrium conditions predicted by Eqs. (11) and (12) and was independent of the electrode electrical conductivity σ_e. Beyond the critical dimensionless scan rate $\Pi_{3,cr}$, predicted values of C_s decreased rapidly with increasing Π_3. In addition, $\Pi_{3,cr}$ increased significantly with increasing electrode electrical conductivity σ_e. Fig. 9 established

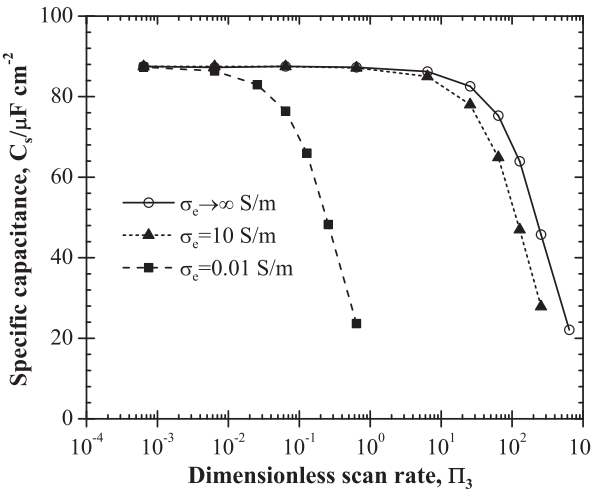

Fig. 9. Predicted specific capacitance from CV simulations as a function of dimensionless scan rate Π_3 for three cases corresponding to $\sigma_e \to \infty$, $\sigma_e = 10$, and 0.01 S/m. Results were obtained by numerically solving the MPNP model with a Stern layer [Eqs. (8) and (9)] accounting for the electrode with $L_e = 100$ nm.

that the electrode electrical conductivity does not affect the double layer capacitance retrieved from CV measurements at low scan rates. However, it significantly affects the measured capacitance at large scan rates which reflects the charging rate performance of EDLCs.

5. Conclusions

This paper presented numerical simulations of cyclic voltammetry measurements for determining the electric double layer capacitance near a planar electrode in aqueous electrolyte solutions. For the first time, a modified Poisson–Nernst–Planck model accounting for the Stern layer was used to simulate the transient double layer dynamics under large electrolyte concentration and electric potential while simultaneously accounting for the electrode electrical conductivity. A dimensional analysis was also first performed for CV measurements based on the model. The following conclusions can be drawn:

1. Four dimensionless numbers were identified to govern the electron and ion transport in the charging dynamics of electric double layers for planar electrode during CV measurements, namely,

$$\Pi_1 = \frac{R_u T/zF}{\psi_{max} - \psi_{min}}, \quad \Pi_2 = \frac{\lambda_D}{L_i}, \quad \Pi_3 = \frac{\nu L^2/D}{\psi_{max} - \psi_{min}},$$

$$\Pi_4 = \frac{\sigma_e(\psi_{max} - \psi_{min})/L_e}{2zeN_A Dc_\infty/L_i}$$

2. For electrodes with large radius of curvature, the hump observed in CV curves was due to the saturation of ion concentration at the electrode surface as the electric potential increased.
3. The predicted EDL capacitance from CV simulations was constant and equal to the capacitance under equilibrium conditions for dimensionless scan rate $\Pi_3 < 1$.
4. The electrode had no effect on the EDL capacitance measured at scan rates smaller than a critical value.

The model developed here can be readily extended to simulate the charging/discharging of mesoporous EDLCs by accounting for the three-dimensional electrode architecture [83,84]. In fact, the above governing equations and boundary conditions remain valid for mesoporous electrodes as long as continuum theory is valid. The latter has been examined in the literature [85–88] and is typically accepted when the pore diameter is larger than 3–5 nm [85–88]. Then, the model can be used to identify the optimum electrode architecture to achieve maximum capacitance and charging performance.

Acknowledgements

This material is based upon work supported as part of the Molecularly Engineered Energy Materials, an Energy Frontier Research Center funded by the U.S. Department of Energy, Office of Science, Office of Basic Energy Sciences under Award Number DE-SC0001342.

References

[1] A.J. Bard, L.R. Faulkner, Electrochemical Methods: Fundamentals and Applications, John Wiley & Sons, New York, NY, 2001.
[2] R.G. Compton, C.E. Banks, Understanding Voltammetry, World Scientific, Hackensack, NJ, 2007.
[3] B.E. Conway, Electrochemical Supercapacitors: Scientific Fundamentals and Technological Applications, Kluwer Academic/Plenum Publishers, New York, NY, 1999.
[4] E. Frackowiak, F. Beguin, Carbon 39 (2001) 937.
[5] D. Pech, M. Brunet, H. Durou, P. Huang, V. Mochalin, Y. Gogotsi, P.L. Taberna, P. Simon, Nat. Nanotechnol. 5 (2010) 651.
[6] K. Xu, Chem. Rev. 104 (2004) 4303.
[7] S.W. Lee, N. Yabuuchi, B.M. Gallant, Nat. Nanotechnol. 5 (2010) 531.
[8] F. Zhao, R.C. Slade, J.R. Varcoe, Chem. Soc. Rev. 38 (2009) 1926.
[9] M.B. Pomfret, J.C. Owrutsky, R.A. Walker, Ann. Rev. Anal. Chem. 3 (2010) 151.
[10] R.J. Hunter, Foundations of Colloid Science, 2nd ed., Oxford University Press, New York, NY, 2001.
[11] J.H. Masliyah, S. Bhattacharjee, Electrokinetic and Colloid Transport Phenomena, John Wiley & Sons, Hoboken, NJ, 2006.
[12] H.J. Butt, M. Kappl, Surface and Interfacial Forces, Wiley-VCH Verlag GmbH & Co. KGaA, Weinheim, Germany, 2010.
[13] W.G. Pell, B.E. Conway, J. Electroanal. Chem. 500 (2001) 121.
[14] I. Kovalenko, D.G. Bucknall, G. Yushin, Adv. Funct. Mater. 30 (2010) 3979.
[15] H. Wang, H.S. Casalongue, Y. Liang, H. Dai, J. Am. Chem. Soc. 132 (2010) 7472.
[16] J. Yan, T. Wei, B. Shao, F. Ma, Z. Fan, M. Zhang, C. Zheng, Y. Shang, W. Qian, F. Wei, Carbon 48 (2010) 1731.
[17] H.R. Byon, S.W. Lee, S. Chen, P.T. Hammond, Y. Shao-Horn, Carbon 49 (2011) 457.
[18] G. Salitra, A. Soffer, L. Eliad, Y. Cohen, D. Aurbach, J. Electrochem. Soc. 147 (2000) 2486.
[19] J. Chmiola, C. Largeot, P.L. Taberna, P. Simon, Y. Gogotsi, Angew. Chem. Int. Ed. 47 (2008) 3392.
[20] D. Aurbach, M.D. Levi, G. Salitra, N. Levy, E. Pollak, J. Muthu, J. Electrochem. Soc. 155 (2008) 745.
[21] R. Lin, P.L. Taberna, J. Chmiola, D. Guay, Y. Gogotsi, P. Simon, J. Electrochem. Soc. 156 (2009) 7.
[22] R. Lin, P. Huang, J. Segalini, C. Largeot, P.L. Taberna, J. Chmiola, Y. Gogotsi, P. Simon, Electrochim. Acta 54 (2009) 7025.
[23] W.G. Pell, B.E. Conway, N. Marincic, J. Electroanal. Chem. 491 (2000) 9.
[24] J. Chmiola, C. Largeot, P.L. Taberna, P. Simon, Y. Gogotsi, Science 328 (2010) 480.
[25] M. Inagaki, H. Konno, O. Tanaike, J. Power Sources 195 (2010) 7880.
[26] F. Béguin, K. Szostak, G. Lota, E. Frackowiak, Adv. Mater. 17 (2005) 2380.
[27] D. Hulicova, J. Yamashita, Y. Soneda, H. Hatori, M. Kodama, Chem. Mater. 17 (2005) 1241.
[28] H.A. Andreas, B.E. Conway, Electrochim. Acta 51 (2006) 6510.
[29] W. Li, D. Chen, Z. Li, Y. Shi, Y. Wan, J. Huang, J. Yang, D. Zhao, Z. Jiang, Electrochem. Commun. 9 (2007) 569.
[30] B. Xu, F. Wu, R. Chen, G. Cao, S. Chen, Z. Zhou, Y. Yang, Electrochem. Commun. 10 (2008) 795.
[31] T. Wang, A. Kiebele, J. Ma, S. Mhaisalkar, G. Gruner, J. Electrochem. Soc. 158 (2011) 1.
[32] M. Kawaguchi, A. Itoh, S. Yagi, H. Oda, J. Power Sources 172 (2007) 481.
[33] M. Seredych, D. Hulicova-Jurcakova, G.Q. Lu, T.J. Bandosz, Carbon 46 (2008) 1475.
[34] H. Konno, H. Onishi, N. Yoshizawa, K. Azumi, J. Power Sources 195 (2010) 667.
[35] R. Mysyk, E. Raymundo-Pinero, J. Pernak, F. Béguin, J. Phys. Chem. C 113 (2009) 13443.
[36] R. Mysyk, E. Raymundo-Pinero, F. Béguin, Electrochem. Commun. 11 (2009) 554.
[37] W.G. Pell, B.E. Conway, J. Power Sources 96 (2001) 57.
[38] F. Fabregat-Santiago, I. Mora-Sero, G. Garcia-Belmonte, J. Bisquert, J. Phys. Chem. B 107 (2003) 758.
[39] W. Lajnef, J.M. Vinassa, O. Briat, S. Azzopardi, E. Woirgard, J. Power Sources 168 (2007) 553.
[40] J.D. Norton, H.S. White, S.W. Feldberg, J. Phys. Chem. 94 (1990) 6772.
[41] C.P. Smith, H.S. White, Anal. Chem. 65 (1993) 3343.

[42] M. Ciszkowska, Z. Stojek, J. Electroanal. Chem. 466 (1999) 129.
[43] M.Z. Bazant, K. Thornton, A. Ajdari, Phys. Rev. E 70 (2004) 1 (No. 021506).
[44] K.T. Chu, M.Z. Bazant, Phys. Rev. E 74 (2006) 1 (No. 011501).
[45] L.H. Olesen, M.Z. Bazant, H. Bruus, Phy. Rev. E 82 (2010) 1 (No. 011501).
[46] H. Wang, L. Pilon, Electrochim. Acta (2012), doi:10.1016/j.electacta.2011.12.051, in press.
[47] E.J.F. Dickinson, R.G. Compton, J. Electroanal. Chem. 655 (2011) 23.
[48] M.S. Kilic, M.Z. Bazant, A. Ajdari, Phys. Rev. E 75 (2007) 1 (No. 021503).
[49] M.Z. Bazant, M.S. Kilic, B.D. Storey, A. Ajdari, Adv. Colloid Interface Sci. 152 (2009) 48.
[50] J. Sanchez-Gonzalez, F. Stoeckli, T.A. Centeno, J. Electroanal. Chem. 657 (2011) 176.
[51] A.G. Pandolfo, A.F. Hollenkamp, J. Power Sources 157 (2006) 11.
[52] L.L. Zhang, X.S. Zhao, Chem. Soc. Rev. 38 (2009) 2520.
[53] L.L. Zhang, R. Zhou, X.S. Zhao, J. Mater. Chem. 20 (2010) 5983.
[54] M.D. Stoller, S. Park, Y. Zhu, J. An, R.S. Ruoff, Nano Lett. 8 (2008) 3498.
[55] M. van Soestbergen, P.M. Biesheuvel, M.Z. Bazant, Phys. Rev. E 81 (2010) 1 (No. 021503).
[56] J. Lim, J. Whitcomb, J. Boyda, J. Varghese, J. Colloid Interface Sci. 305 (2007) 159.
[57] I. Rubinstein, B. Zaltzman, Adv. Colloid Interface Sci. 159 (2010) 117.
[58] J.N. Israelachvili, Intermolecular and Surface Forces, 3rd ed., Academic Press, San Diego, CA, 2010.
[59] D.J. Griffiths, Introduction to Electrodynamics, 3rd ed., Prentice Hall, Upper Saddle River, NJ, 1999.
[60] R.P. Feynman, R.B. Leighton, M. Sands, The Feynman Lectures on Physics, vol. 2, 2nd ed., Addison Wesley, New York, NY, 2005.
[61] Y.-H. Chen, C.-W. Wang, X. Zhang, A.M. Sastry, J. Power Sources 195 (2010) 2851.
[62] A.M. Colclasure, R.J. Kee, Electrochim. Acta 55 (2010) 8960.
[63] C.Y. Wang, Chem. Rev. 104 (2004) 4727.
[64] P.P. Mukherjee, G. Wang, C.Y. Wang, in: R. White, C. Vayenas, M. Gamboa-Aldeco (Eds.), Modern Aspects of Electrochemistry, No. 40, Springer, New York, NY, 2007, pp. 285–341.
[65] T. Berning, D.M. Lu, N. Djilali, J. Power Sources 106 (2002) 284.
[66] M.S. Kilic, M.Z. Bazant, A. Ajdari, Phys. Rev. E 75 (2007) 1 (No. 021502).
[67] H. Wang, L. Pilon, J. Phys. Chem. C 115 (2011) 16711.
[68] H.C. Yeh, R.J. Yang, W.-J. Luo, Phys. Rev. E 83 (2011) 1 (No. 056326).
[69] J. Lyklema, Fundamentals of Interface and Colloid Science, Vol. II: Solid–Liquid Interfaces, Academic Press, San Diego, CA, 2001.
[70] D.R. Lide (Ed.), CRC Handbook of Chemistry and Physics, 90th ed., CRC Press/Taylor & Francis, Boca Raton, FL, 2010.
[71] H. Cohen, J.W. Cooley, Biophys. J. 5 (1965) 145.
[72] T.R. Brumleve, R.P. Buck, J. Electroanal. Chem. 90 (1978) 1.
[73] T.R. Brumleve, R.P. Buck, J. Electroanal. Chem. 126 (1981) 73.
[74] J.R. Macdonald, J. Chem. Phys. 58 (1973) 4982.
[75] R.P. Buck, J. Membr. Sci. 17 (1984) 1.
[76] F. Beunis, F. Strubbe, M. Marescaux, J. Beeckman, K. Neyts, A.R.M. Verschueren, Phys. Rev. E 78 (2008) 1 (No. 011502).
[77] J.J. Yoo, K. Balakrishnan, J. Huang, V. Meunier, B.G. Sumpter, A. Srivastava, M. Conway, A.L.M. Reddy, J. Yu, R. Vajta, P.M. Ajayan, Nano Lett. 11 (2011) 1423.
[78] J.S. Newman, K.E. Thomas-Alyea, Electrochemical Systems, 3rd ed., John Wiley & Sons, Hoboken, N.J, 2004.
[79] R.P. Buck, J. Electroanal. Chem. 210 (1986) 1.
[80] J. Huang, B.G. Sumpter, V. Meunier, Angew. Chem. Int. Ed. 47 (2008) 520.
[81] J. Huang, B.G. Sumpter, V. Meunier, Chem. Eur. J. 14 (2008) 6614.
[82] J. Huang, B.G. Sumpter, V. Meunier, G. Yushin, C. Portet, Y. Gogotsi, J. Mater. Res. 25 (2010) 1525.
[83] H. Wang, J. Varghese, L. Pilon, Electrochim. Acta 56 (2011) 6189.
[84] J. Varghese, H. Wang, L. Pilon, J. Electrochem. Soc. 158 (2011) 1106.
[85] R. Qiao, N.R. Aluru, J. Chem. Phys. 118 (2003) 4692.
[86] H. Daiguji, Chem. Soc. Rev. 39 (2010) 901.
[87] J.C.T. Eijkel, A. van den Berg, Chem. Soc. Rev. 39 (2010) 957.
[88] W. Sparreboom, A. van den Berg, J.C.T. Eijkel, New J. Phys. 12 (2010) 1 (No. 015004).